Journal of Cancer Research and Clinical Oncology (2019) 145:685–694
https://doi.org/10.1007/s00432-018-02827-6

ORIGINAL ARTICLE – CANCER RESEARCH

FTIR-based spectrum of salivary exosomes coupled with computational-aided discriminating analysis in the diagnosis of oral cancer

Ayelet Zlotogorski-Hurvitz[1,2] · Ben Zion Dekel[3] · Dov Malonek[3] · Ran Yahalom[4] · Marilena Vered[1,5]

Received: 9 November 2018 / Accepted: 15 December 2018 / Published online: 3 January 2019

Abstract

Purpose To determine the Fourier-transform infrared (FTIR) spectra of salivary exosomes from oral cancer (OC) patients and healthy individuals (HI) and to assess its diagnostic potential using computational-aided models.

Methods Whole saliva samples were collected from 21 OC patients and 13 HI. Exosomes were pelleted using differential centrifugation (12,000*g*, 120,000*g*). The mid-infrared (IR) absorbance spectra (900–5000 cm^{-1} range) were measured using MIR8025 Oriel Fourier-transform IR equipped with a PIKE MIRacle ZnSe attenuated total reflectance attachment. Machine learning techniques, utilized to build discrimination models for the absorbance data of OC and HI, included the principal component analysis–linear discriminant analysis (PCA–LDA) and support vector machine (SVM) classification. Sensitivity, specificity and the area under the receiver operating characteristic curve were calculated.

Results IR spectra of OC were consistently different from HI at 1072 cm^{-1} (nucleic acids), 2924 cm^{-1} and 2854 cm^{-1} (membranous lipids), and 1543 cm^{-1} (transmembrane proteins). The PCA–LDA discrimination model correctly classified the samples with a sensitivity of 100%, specificity of 89% and accuracy of 95%, and the SVM showed a training accuracy of 100% and a cross-validation accuracy of 89%.

Conclusion We showed the specific IR spectral signature for OC salivary exosomes, which was accurately differentiated from HI exosomes based on detecting subtle changes in the conformations of proteins, lipids and nucleic acids using optimized artificial neural networks with small data sets. This non-invasive method should be further investigated for diagnosis of oral cancer at its very early stages or in oral lesions with potential for malignant transformation.

Keywords Oral cancer · Saliva · Exosomes · Fourier-transform infrared (FTIR) · Machine learning · Diagnosis

Introduction

Oral cancer (OC), referring to the main variant of squamous cell carcinoma, is now assessed to have a global incidence of over 300,000 new annual cases with a trend to further increase in younger patients and in developing countries (Ferlay et al. 2015; Shield et al. 2017). The 5-year prognosis has not substantially changed for more than 4 decades and stands as low as 50%. One of the caveats associated with OC is the ability to identify early changes in the oral lining epithelium, mainly in those patients at high risk to develop OC.

Tissue biopsy and light microscopy are still the gold-standard diagnostic tools. However, these are performed when lesions (cancerous or pre-cancerous) are visible and already contain substantial genetic changes. Moreover, tissue biopsies provide information that is limited to a portion of a tumor and at a specific time-point. Liquid biopsy, based on

✉ Marilena Vered
mvered@post.tau.ac.il

1 Department of Oral Pathology and Oral Medicine, School of Dentistry, Tel Aviv University, 69978 Tel Aviv, Israel

2 Department of Oral and Maxillofacial Surgery, Rabin Medical Center, Petah Tikva, Israel

3 Department of Electrical and Computer Engineering, Ruppin Academic Center, Emek Hefer, Israel

4 Department of Oral and Maxillofacial Surgery, The Chaim Sheba Medical Center, Tel Hashomer, Israel

5 Institute of Pathology, The Chaim Sheba Medical Center, Tel Hashomer, Israel

different body fluids, is currently a new concept in cancer diagnostics as it can provide information at successive time points on circulating tumor cells, DNA/RNA molecules and extracellular microvesicles which conform to the plasticity of tumor behavior (Lousada-Fernandez et al. 2018; Wong and Nonaka 2018). In this line, saliva can be used as a promising biofluid for the early identification of biomarkers for both local and systemic diseases. Saliva has the advantages of accessibility and repeatability that minimize the need for invasive and painful procedures or sophisticated technical devices (Katsiougiannis et al. 2017; Lau et al. 2013; Malamud 2011).

Exosomes are 30–100-nm membrane-bound nanovesicles produced by the endosomal pathway in both normal and cancerous cells, and released through exocytosis to the extracellular space and circulation (Mathiavanan et al. 2010; Vlassov et al. 2012). Molecularly, exosomes express specific markers such as tetraspanins (i.e., CD63, CD9, and CD81), Alix, TSG101, and heat shock proteins. Functionally, they have been associated with the transfer of variable proteins, lipids, mRNAs and microRNAs that reflect the cytosol content of their parental cells (Mathivanan et al. 2010; Simons and Raposo 2009). Salivary exosomes, have been isolated from oral cancer patients and were shown to demonstrate characteristic morphological and molecular features different from those of healthy individuals (Palanisamy et al. 2010; Zlotogorski-Hurvitz et al. 2016).

Infrared (IR) spectroscopy is a non-destructive method that can investigate solid tissues, fluids and cells. It acts on the principle of vibrating molecular bonds and the resulting absorption wavelengths, which depend on the involved atoms and strength of intermolecular interactions, determine the chemical profile of a specific material. Therefore, as recently shown, Fourier-transform IR (FTIR) spectroscopy coupled with computational methods can provide fingerprint spectra of benign tissues and their counterpart malignant tumors with a high rate of accuracy (Baker et al. 2008; Dukor 2006; Li et al. 2017; Simanova and Karamancheva 2013).

Our aim was to use FTIR spectroscopy combined with machine learning methods for the primary evaluation of the characteristic spectra of salivary exosomes from OC patients and healthy individuals (HI), thus creating a novel platform for the application of FTIR spectroscopy for the early diagnosis of oral cancer.

Materials and methods

Study population

The study included patients diagnosed with oral cancer (OC) at the Oral and Maxillofacial Department, Sheba Medical Center, between the years 2015 and 2016. In addition, healthy individuals without OC (i.e., HI) were also recruited for the study. The study was approved by the IRB of the Medical Center. All patients and healthy individuals involved in the study signed the informed consent form.

Unstimulated whole saliva was collected from OC patients prior to any anti-cancer treatment. In regard to HI, all subjects were selected after a thorough examination of the oral cavity by a specialist in oral medicine (AZH), who excluded the existence of any pathological lesions. The collected saliva was immediately centrifuged at 3000×*g* for 20 min at 4 °C for the elimination of macromolecules, as previously described (Zlotogorski-Hurvitz et al. 2015). Since the volumes of saliva collected from part of the OC patients were limited (0.5–1 ml) and were further reduced following centrifugation, these individual samples ($N=8$) were pooled into one sample. The remaining samples ($N=9$) were handled individually. Similarly, in the HI group, part of the samples was managed separately ($N=5$) and the rest were joined into one pooled sample composed of eight individual samples. The supernatant of all samples was kept at − 70 °C until further use.

Nanoparticle tracking analysis (NTA)

The cleaned saliva was centrifuged at 12,000×*g* for 20 min to further remove residual organelles and cell fragments. Randomly selected, aliquots (1 ml) of three individual OC and HI samples of saliva, each, were 1:1 diluted with phosphate buffered saline (PBS). Each of these were run for three times and were analyzed by measuring the rate of Brownian motion using a NanoSight NS300 system (NanoSight Ltd., Malvern, UK), as previously described (Vlassov et al. 2012). Resulting particle concentrations were averaged across samples from the same dilution. The results were expressed as the average concentration per 1 ml ± SD and the average modal size ± SD (nm) of the nanoparticles.

Exosome isolation from saliva

Following the initial centrifugation steps, 1 ml supernatant of each sample was transferred to 1.0-ml polycarbonate tubes for ultracentrifugation at 120,000×*g* for 70 min at 4 °C (Beckman Coulter Optima TLX, TLA 120.2 rotor) (Krafft et al. 2017; Mihaly et al. 2017). After removal of the supernatant, all pellets were kept in PBS at − 70 °C until further analysis.

Transmission electron microscope (TEM)

The pooled exosomal pellets (HI and OC) were fixed in 500 µl of 2.5% glutaraldehyde in 5% sucrose and 0.1 M sodium cacodylate at pH 7.4 for 30 min at room temperature,

after which 1% osmium tetroxide was added for 90 min followed by dehydration and fixation with epoxy resin. Ultrathin sections were placed on nickel grids and further stained with uranyl acetate and lead citrate. The sections were examined by a TEM (JEOL TEM JEM 1200EX, Peabody, MA, USA).

Western Blotting (WB)

WB procedures were performed on the pooled samples as detailed previously (Zlotogorski-Hurvitz et al. 2015). Briefly, exosomal pellets were treated with RIPA buffer and protease inhibitors (both from Sigma-Aldrich). Approximately 40 µg total protein was separated in reducing conditions with 2-mercaptoethanol (AMRESCO, Solon, OH, USA) on 12% sodium dodecyl sulfate-polyacrylamide gel electrophoresis (SDS-PAGE). Nitrocellulose membranes (Whatman, Sigma-Aldrich) were incubated with primary antibodies (1:1,000, Cat# EXOAB-CD63A-1, EXOAB-CD9A-1, and EXOAB-CD81A-1, System Biosciences Inc., Palo Alto, CA, USA) and secondary antibody HRP-labeled goat anti-rabbit IgG (1:20,000, System Biosciences), and finally visualized using the enhanced chemiluminescence (ECL) detection system (GE Healthcare Buckinghamshire, UK).

Fourier-transform infrared (FTIR) spectroscopy

FTIR analysis was performed on all individual samples as well as on the pooled samples. FTIR spectra were collected using MIR 8025 FTIR spectrometer (Newport-Oriel, Irvine, California, USA) equipped with a liquid nitrogen cooled mercury–cadmium–telluride (MCT) detector. The spectra were collected in attenuated total reflection (ATR) mode using a 3-reflection MIRacle ATR ZnSe Crystal (PIKE technologies, Fitchburg, WI, USA).

Frozen samples were thawed at room temperature for approximately 5 min. Prior to the measurement of every new sample, the ATR crystal was cleaned with ethanol and a background measurement was acquired. The sample pellet was put on the ZnSe ATR crystal and the PBS buffer solvent was slowly de-hydrated with low-pressure flow of pure nitrogen gas. As for the reference measurement, PBS was put on the ZnSe ATR crystal and a thin dry PBS film was obtained by slowly evaporating the water from the PBS. Measurements were performed at room temperature, immediately after drying the sample (within approximately 2 min). The nominal resolution was 8 cm^{-1} and the wavenumber range was from 900 to 5000 cm^{-1}. To increase signal to noise ratio, 150 scans were co-added for each measurement.

Upon completing the spectral measurement, absorption spectra were calculated using the ATR sample and background spectra. Finally, the PBS absorption spectrum was subtracted from the sample absorption spectra. The method by which PBS spectra were subtracted was based on the assumption that spectral lines of lipids at 2850 cm^{-1} and 2930 cm^{-1} are unique only to the exosomes and not to the PBS, so a multiplication factor was chosen such that after the subtraction of the two spectra, the absorption between 2850 and 2930 cm^{-1} will take into account only the lipid absorption lines. The calculated absorption spectra were saved for additional spectral processing steps and for later use to build discrimination models.

Data processing was carried out using MATLAB (Mathworks, Natick, MA, USA) and Unscrambler (Camo, Oslo, Norway) packages.

Spectra preprocessing

Two preprocessing methods were performed on all FTIR spectra. First, the Savitsky–Golay smoothing algorithm with a window width of five points was applied to each spectrum, to reduce random noise in the data. Then, each absorbance spectrum was normalized to the height of amide I absorbance band at ~ 1650 cm^{-1}.

Spectra processing method

Absorbance spectra were processed by two methods. First, mean absorbance spectrum of each group was calculated. Absorbance peaks, which differed significantly between the two groups, were identified by visual inspection. Ratios between heights of those peaks were calculated and t-test was performed to calculate the significance of differences between those groups (significance was set at $p < 0.05$). Second, machine learning techniques were utilized to build discrimination models between the two groups: principal component analysis–linear discriminant analysis (PCA–LDA) and support vector machine (SVM) classification. K-fold cross-validation (Fushiki 2011) was employed to estimate the accuracy of the discrimination models: the data were randomly partitioned into five equal-sized subsamples. A single subsample was used as the validation data for testing the model, and the remaining four subsamples were used as training data. The process was repeated five times, with each of the subsamples used once as the validation data. The results were then averaged to produce a single value. Sensitivity, specificity and the area under the receiver operating characteristic curve were calculated.

Results

Study groups

HI comprised of 10 males and 3 females, age range between 28 and 52 years; OC group comprised of 13

males and 8 females, age range between 38 and 81 years. Ten patients were in early stage (T1-2/N0M0) and the rest in advanced stage of disease. Patients were followed up for at least 24 months, during which two have died of disease, while the rest showed no evidence of disease (Table 1).

Characterization of the exosomal samples

NTA analysis showed a population of nanoparticles with a median mode of 109.8 ± 4.8 nm for the OC samples and a median mode of 84.1 ± 6.2 nm for the HI samples (Fig. 1a, b, respectively). The curve of the OC showed an expanded range, as it encompassed a sub-population of nanoparticles of considerably larger diameters compared to those of HI.

Table 1 Demographic data and clinical findings of healthy individuals and patients with oral cancer

Study group	Age	Gender	Location of tumor	Clinical stage	Medical background related to the oral mucosa	Current survival status
Healthy individuals	46	M	–	–	–	–
	36	M	–	–	–	–
	36	M	–	–	–	–
	51	F	–	–	–	–
	47	M	–	–	–	–
	44	M	–	–	–	–
	35	M	–	–	–	–
	28	M	–	–	–	–
	41[a]	F	–	–	–	–
	41[a]	M	–	–	–	–
	48[a]	F	–	–	–	–
	52[a]	M	–	–	–	–
	45[a]	M	–	–	–	–
Oral cancer patients	78	M	Mandibular gingiva	2	–	NED
	68	M	Mandibular alveolar mucosa and floor of mouth	2	Proliferative verrucous leukoplakia	NED
	60	M	Tongue	1	–	NED
	79	M	Mandibular gingiva	2	–	NED
	38	F	Tongue and floor of mouth	2	–	NED
	63	F	Tongue and floor of mouth	1	–	NED
	65	M	Mandibular vestibule	2	–	NED
	75	M	Tongue	1	–	NED
	81	M	Mandibular alveolar mucosa, buccal mucosa, soft palate	2	–	NED
	56 [b]	M	Maxillary alveolar mucosa	2	–	NED
	61[b]	M	Tongue	1	Lichen planus	NED
	51[b]	M	Buccal mucosa	1	–	NED
	41[b]	M	Mandibular alveolar mucosa	1	Lichen planus	NED
	54[b]	F	Tongue	1	–	NED
	69[b]	M	Tongue	2	–	Dead of disease
	67[b]	F	Mandibular alveolar mucosa	1	Lichen planus	NED
	60[b]	F	Maxillary alveolar mucosa	2	–	NED
	65[b]	F	Maxillary alveolar mucosa	2	–	NED
	68[b]	M	Tongue	1	–	NED
	65[b]	F	Mandibular alveolar mucosa	1	–	NED
	57[b]	F	Tongue and floor of mouth	2	–	Dead of disease

M male, *F* female; *Clinical stage 1* T1/2N0M0, *Clinical stage 2* T > 2N > 0M0, *NED* no evidence of disease

[a]Exosomal pellet contained pooled saliva from five healthy individuals

[b]Exosomal pellet contained pooled saliva from eight patients with oral cancer

TEM examination demonstrated characteristic morphological features of exosomal particles for both the OC and HI isolates (Fig. 1c, d). These highlighted round-to-oval-shaped particles bounded by a bi-layer membrane.

WB of OC and HI pellets showed expression of well-recognized exosomal markers, CD9, CD81 and CD63 (Fig. 1e), which support the classification of the isolated microvesicles as exosomes. These markers were differentially expressed in OC and HI: the CD63 band at ~53 kDa was more prominent in OC compared to HI. The CD81 and CD9, with recognized bands at 26 and 28 kDa, respectively, were more pronounced in HI compared to OC. These patterns were previously reported by us (Zlotogorski-Hurvitz et al. 2015) and others (Sharma et al. 2011; Vlassov et al. 2012).

Analysis of FTIR-ATR spectra

Differences were observed in the FTIR-ATR spectra of saliva-derived exosomes between those isolated from OC patients and from HI. These differences occurred in biomolecules that constitute carbohydrates, nucleic acids, proteins and lipids. The entire absorbance spectra (range 950–3650 cm^{-1}) of the OC and HI exosomes are illustrated in Fig. 2a.

The enlarged spectral profile of OC exosomes showed a peak of absorbance intensity at 1033 cm^{-1} (Fig. 2b). Bands in this area are responsible for the vibrational modes of –CH2OH groups and the C–O stretching vibration coupled with C–O bending of the C–OH groups of carbohydrates (i.e., glucose, fructose and glycogen) (Simanova and Karamancheva 2013; Zelig et al. 2011). The peak of HI exosomes in this region was slightly higher.

HI and OC exosomes showed a peak of absorbance intensity at 1072 cm^{-1} with that of OC being lower compared to HI (Fig. 2b). This is the region of the symmetric stretching modes of the phosphodiester groups of cellular nucleic acids of DNA and RNA (Gao et al. 2015; Simanova and Karamancheva 2013; Zelig et al. 2011).

The relative intensity ratio at 1033 cm^{-1} and 1072 cm^{-1} ($I_{1,033}/I_{1,072}$) was significantly higher for OC (1.36 ± 0.2) compared to HI (1.16 ± 0.12) ($p = 0.024$) (Fig. 3a).

The spectral peaks at 2924 cm^{-1} and 2854 cm^{-1} seen in the HI exosomes are associated with the absorption bands of asymmetric and symmetric C–H stretching vibrations of CH_2 and CH_3 methylene groups, which are contained in fatty acids within cellular membranes (Gao et al. 2015; Simanova and Karamancheva 2013) (Fig. 2c). OC exosomes showed peaks in the same positions; however, they were of a lower intensity compared to those of the HI exosomes. The relative intensity ratio at 2924 cm^{-1} and 2854 cm^{-1} ($I_{2,924}/I_{2,854}$) was significantly higher for OC (1.19 ± 0.37) compared to HI (0.89 ± 0.12) ($p = 0.027$) (Fig. 3b).

The band at 1743 cm^{-1} is attributed C=O stretching vibration in cellular lipids (Gao et al. 2015; Li et al. 2017; Simanova and Karamancheva 2013). The HI exosomes showed a peak of absorbance intensity at this wavenumber, which lacked in the OC exosomes (Fig. 2d). The OC exosome spectrum was of a lower intensity in this region. This contained a series of tiny and irregular peaks, which were most likely associated with the measurement of noise (Fig. 2d).

The protein spectra are positioned in the region of 1300–1800 cm^{-1} wavenumbers (Simanova and Karamancheva 2013). Bands in this region represent mainly

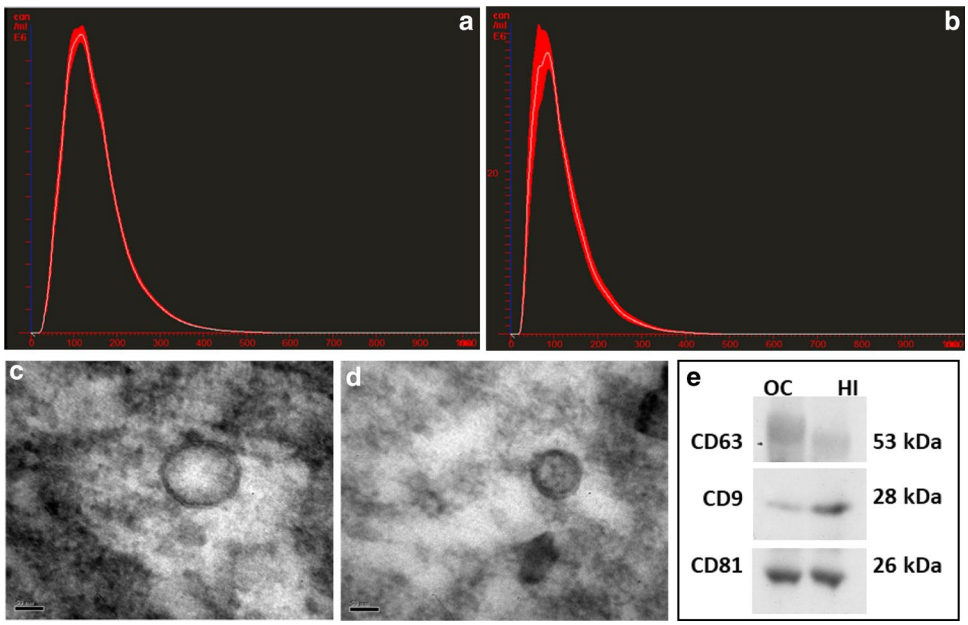

Fig. 1 **a** Average size distribution of nanoparticles in whole saliva of oral cancer patients. **b** Average size distribution of nanoparticles in whole saliva of healthy individuals. **c** Transmission electron microscopy of salivary exosomes highlights the bi-layer membranes in cancer samples. **d** Transmission electron microscopy of salivary exosomes highlights the bi-layer membranes in healthy samples. **e** Western blotting of cancer and healthy exosomal pellet lysates. The molecular weight standards (kDa) are marked on the right

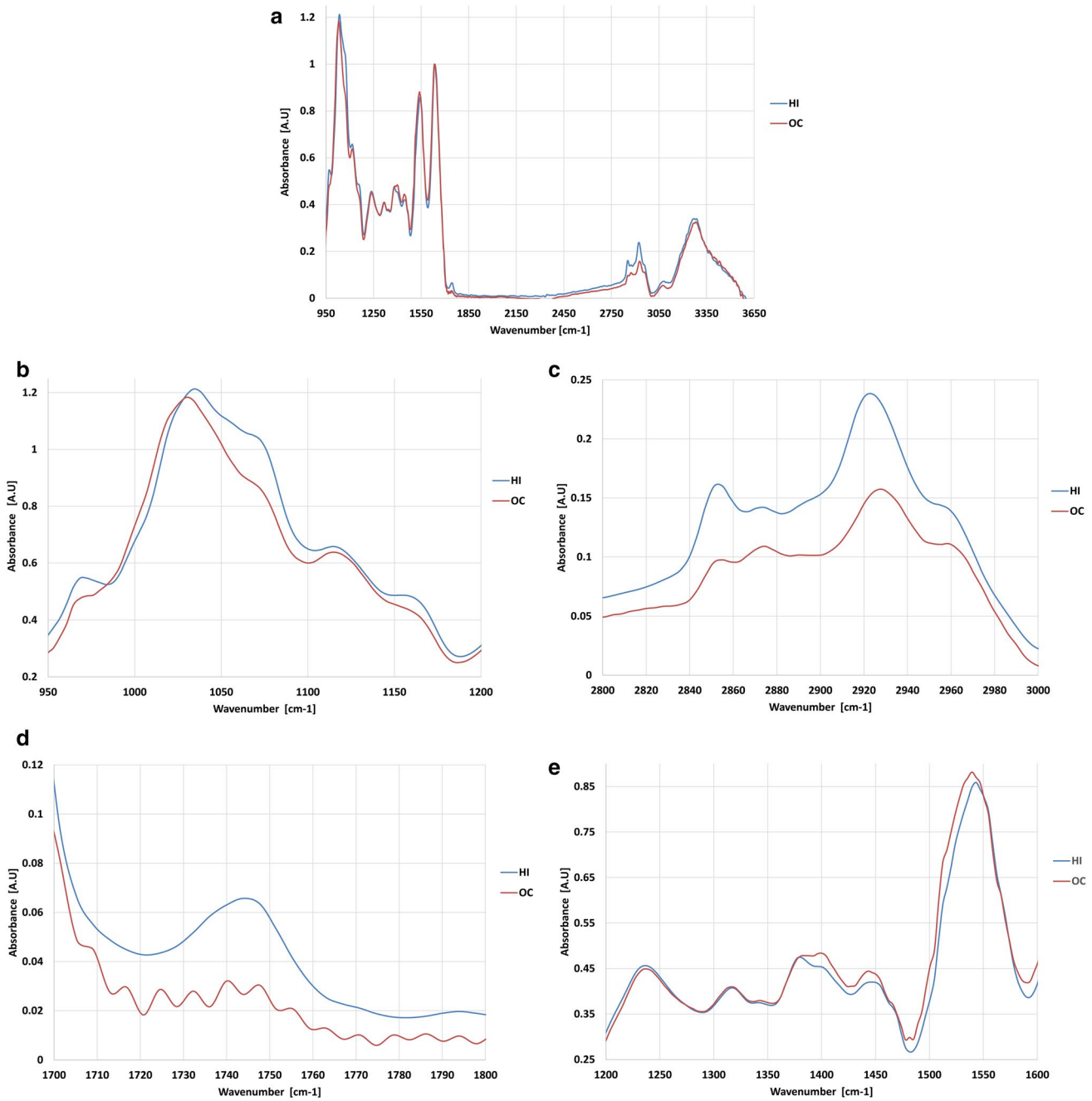

Fig. 2 **a** The entire average absorbance spectra in the range of 950–3650 cm^{-1} of the OC and HI exosomes. **b** The average absorbance spectra in the range 950–1200 cm^{-1} of the OC and HI exosomes. **c** The average absorbance spectra in the range of 2800–3000 cm^{-1} of the OC and HI exosomes. **d** The average absorbance spectra in the range of 1200–1600 cm^{-1} of the OC and HI exosomes. **e** The average absorbance spectra in the range of 1700–1800 cm^{-1} of the OC and HI exosomes

amide II, likely attributed to the region of transmembrane proteins (Dave et al. 2008). In general, the absorbance spectrum of the OC exosomes was of a higher intensity compared to the HI exosomes (Fig. 2e). For OC exosomes, the peak was observed at 1543 cm^{-1}, while the peak of HI exosomes showed a slight shift to the right, being positioned at 1547 cm^{-1}. Another peak in the OC exosomes was seen at 1404 cm^{-1}, which is the region of CH bending vibration bonds in acyl residues of lipids or amines (Christoua et al. 2018; Gao et al. 2015; Simanova and; Karamancheva 2013). The relative intensity ratio at 1404 cm^{-1} and 2924 cm^{-1} ($I_{1,404}/I_{2,924}$) was significantly higher for OC (3.4 ± 1.23) compared to HI (1.97 ± 0.51) ($p = 0.005$) (Fig. 3c).

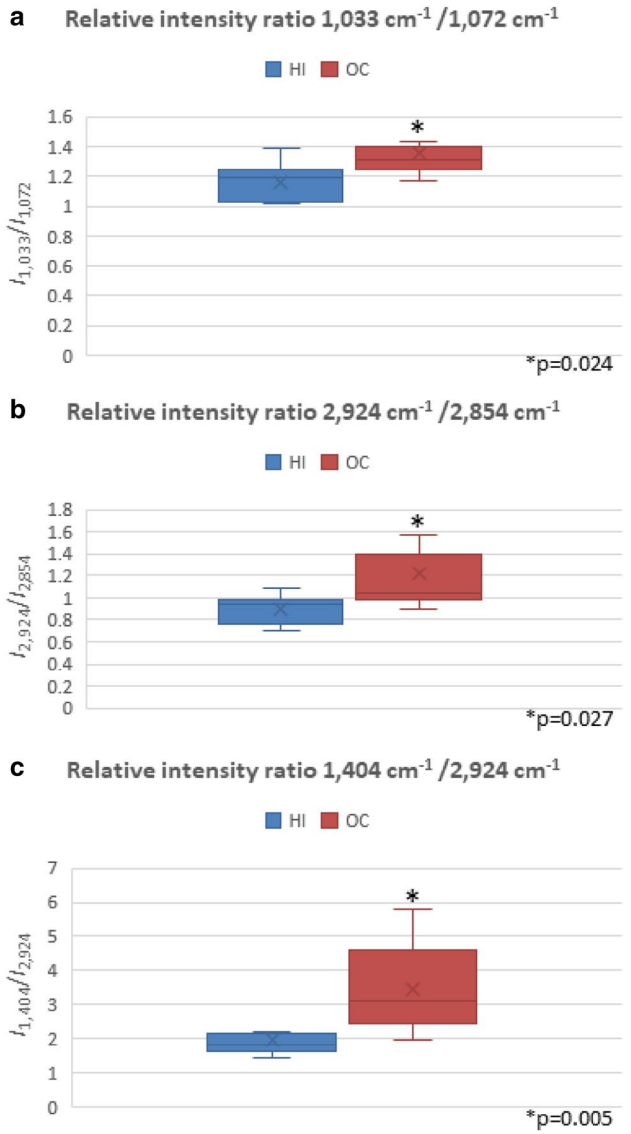

Fig. 3 **a** Relative intensity ratio of 1033 cm^{-1} and 1072 cm^{-1} ($I_{1,033}/I_{1,072}$). **b** Relative intensity ratio of 2924 cm^{-1} and 2854 cm^{-1} ($I_{2,924}/I_{2,854}$). **c** Relative intensity ratio of 1404 cm^{-1} and 2924 cm^{-1} ($I_{1,404}/I_{2,924}$). Boxes and error bars represent mean and range, respectively

Classification analysis and relationship of the spectral signature with clinical data

Two main classification methods were performed, PCA–LDA and SVM. The input was composed of the spectra absorbance bands in the 900 cm^{-1}–3700 cm^{-1}, the ratios of 1037 cm^{-1}/2924 cm^{-1}, 2854 cm^{-1}/2874 cm^{-1} and the area under the absorbance spectrum from 1720 to 1760 cm^{-1}, from 2820 to 3000 cm^{-1} and from 950 to 1500 cm^{-1}. The discriminant PCA–LDA plot showed separation of exosomal pellets from OC patients and HI individuals (Fig. 4a). Although supplied with a small number of samples, the PCA–LDA discrimination model was able to correctly classify the samples with a sensitivity of 100%, specificity of 89% and accuracy of 95%. Only one HI sample was misdiagnosed as OC, as shown in the confusion matrix (Fig. 4b).

The discriminant SVM plot showed also separation of exosomal pellets between OC patients and HI individuals (Fig. 4c). The model was able to correctly classify the samples with a training accuracy of 100% and a cross-validation accuracy of 89%.

Discussion

The present study aimed to use FTIR spectroscopy with ATR to show for the first time the specific spectral signature of salivary exosomes. Furthermore, a discriminant function model (PCA–LDA) could distinguish with high accuracy the spectra of OC exosomes from those of HI exosomes. These differences encompassed changes in the content and/or structure of nucleic acids, lipids and proteins. In spite of these being initial findings, they highlight the value of applying FTIR spectroscopy and optimized algorithms for the diagnosis of oral cancer based on saliva-related nanoparticles. This approach has the advantage of a non-invading method by which examination material can be repeatedly achieved as a factor of the clinical findings or during follow-up periods in high-risk patients.

The peak at 1072 cm^{-1}, corresponding to absorbance bands of phosphate bonds within nucleic acids, reflect the DNA content. In the present study, the band of HI was higher than that in OC. This seems to be contradicting to the findings in other types of cancers, such as colorectal, breast, esophagus, skin and ovary, where peak intensities were higher in malignant tissues than in their normal/non-cancerous counterparts, indicating the increased and uncontrolled replication of DNA, as one of the most important characteristics of cancer (Gao et al. 2015; Simanova and Karamancheva 2013). We could assume that due to the minute fraction of cytosol that is contained within the exosomes, the amounts of nucleic acids do not entirely replicate those found in the parental cells. The reason why the content of nucleic acids in exosomes from cancer patients can be lower than that from exosomes of healthy subjects should be further investigated. In the only other study in which plasma and serum exosomes were investigated by FTIR in prostate cancer patients, there was no reference to this spectral region (Krafft et al. 2017).

The relative intensities between the band of glycogen/carbohydrates (1033 cm^{-1}) and that of nucleic acids (1072 cm^{-1}) were significantly higher in OC than in HI. This could serve as a fingerprint FTIR signature for detection of oral cancer.

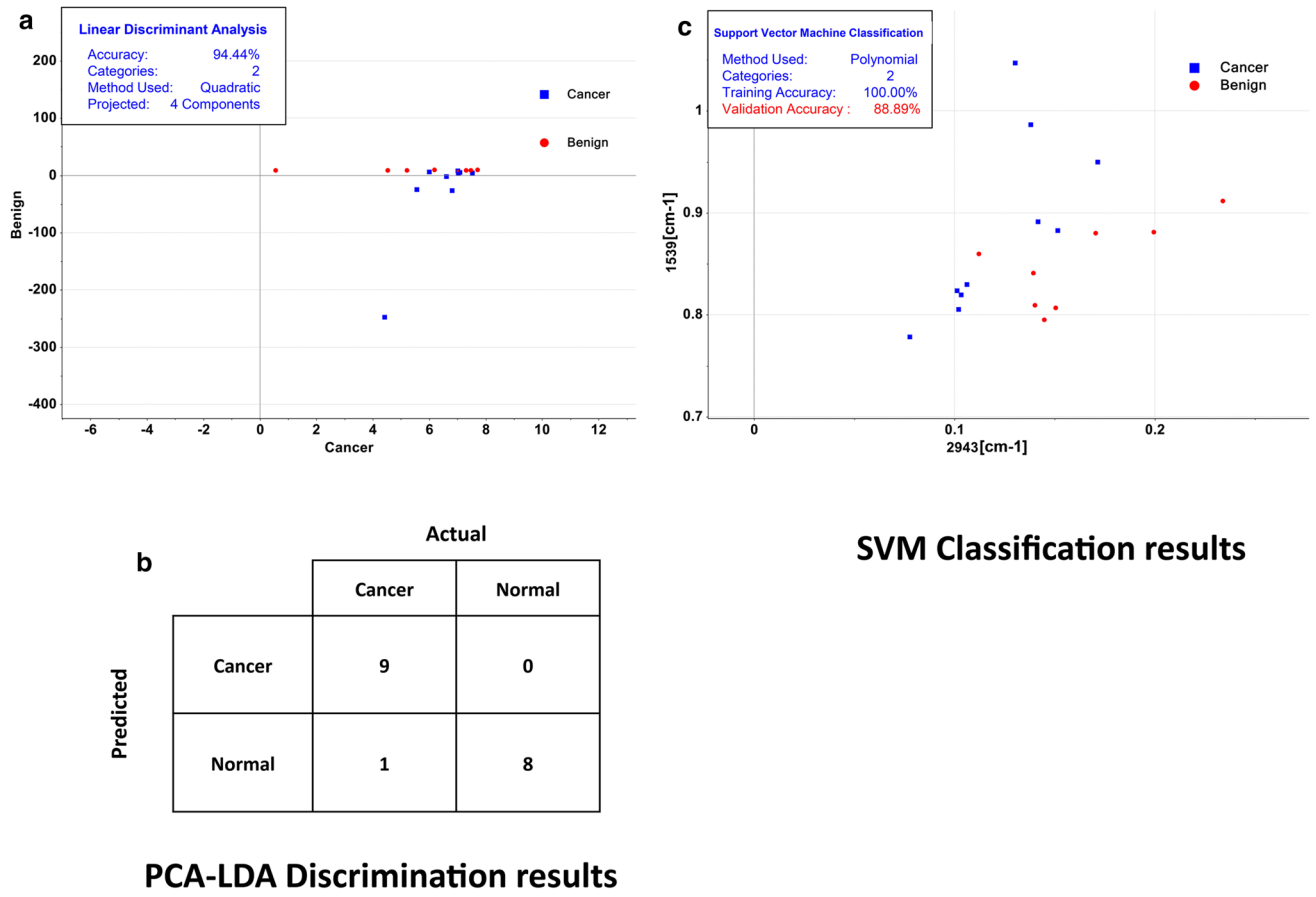

Fig. 4 **a** PCA–LDA discrimination results. **b** PCA–LDA confusion matrix. **c** SVM classification results

The peak absorbance bands at 2924 cm^{-1} and 2854 cm^{-1} correspond to cell membrane lipids (Gao et al. 2015; Simanova and Karamancheva 2013). As exosomes are bounded by the cell membranes of their parental cells, changes found in exosomes are expected to reflect the modifications in the cells of origin. Bands in HI exosomes were higher and stronger than in OC. This was in line with findings from colorectal cancer (Li et al. 2017) but not with ovary and breast cancers (Simanova and Karamancheva 2013), emphasizing the assumption that each type of cancer demonstrates a unique FTIR spectra. The decrease of the FTIR spectra of lipids in OC exosomes can be explained in terms of energy requirements of the cancerous cell, where a high consumption of lipids meets the nutritional needs of rapidly growing and invading cell population (Li et al. 2017). The significant difference in the relative intensities of 2924 cm^{-1} and 2854 cm^{-1} bands between OC and HI can indicate characteristic changes in various lipids that occurred in the membranes of the cancerous cells and their exosomal "derivatives". Furthermore, we found a significantly higher intensity ratio of bands in the region of acyl residues (1404 cm^{-1}) and lipids (2924 cm^{-1}) in OC compared to HI. Membrane lipids are known to be particularly vulnerable to oxidation due to their high content in acyl chains, a process that might lead to remarkable changes in their physico-chemical properties, thereby significantly affecting membrane behavior (Fantini and Yahi 2015). Oxidation of fatty acids in membranous phospholipids perturbs the packing properties of these lipids and modifies their membrane topology. As a result, previously hydrophobic acyl chains buried in the membrane may gain enough polarity to project into the aqueous environment, thus permitting modifications in the interactions among the cell membrane lipids and/or proteins in the same cells or with neighboring cells (Fantini and Yahi 2015). These findings may represent changes that presumably occur in malignant cells.

The main absorbance peak at 1543 cm^{-1} is typical of amine II membrane proteins with oriented secondary-structural components (Dave et al. 2008). According to our findings, salivary exosomes from OC patients showed a higher content of these proteins compared to those from HI. In contrast to the more defined secondary structures of amine I proteins in terms of α-helix and β-sheet regions (Gallagher 2009), there are data that show that amine II can

contain proteins with α-helix structure towards wavenumber 1541 cm^{-1} (Baker et al. 2008) and β-sheet structure towards wavenumber 1550 cm^{-1} (Gao et al. 2015). These could be of major biological significance in cancer since membranal proteins play key roles at both intracellular and intercellular levels, including functions such as channel-regulating peptides, enzymes and receptors (Moore et al. 2008).

Although the study contained a rather low number of subjects, the discrimination function model was able to differentiate OC from HI salivary exosomes with a sensitivity of 100% and specificity of 89%, supporting a valid bio-structural difference between these groups. Even though the population of exosomes in saliva of OC patients is an admixture of nanoparticles released by both the tumor cells and the non-cancerous oral epithelium, the discriminant function model (PCA–LDA) could distinguish with high accuracy the spectra of OC exosomes from those of HI exosomes, indicating that the exclusive features of the cancerous exosomes prevailed (Principe et al. 2013). Interestingly, early- and late-stage oral cancers have been identified in the same cluster, thus supporting the use of FTIR for the diagnosis of oral cancer in the early stages and monitoring risk populations with oral pre-malignant disorders. Its use in following up oral cancer patients should also be investigated due to the increased risk to develop a recurrent tumor or a second primary tumor of the upper aero-digestive tract as a consequence of field cancerization (Mohan and Jagannathan 2014).

In summary, we have shown for the first time the signature of FTIR-based spectrum of salivary exosomes. The present findings are important as they show that cancer exosomes can be accurately differentiated from their benign counterparts based on detecting subtle changes in the conformations of proteins, lipids and nucleic acids using optimized artificial neural networks with small data sets for processing the spectral data. This may have an important role for the development of next-generation techniques for the early diagnosis of oral cancer within the current framework that combines nanoparticles, liquid biopsy diagnostics and artificial intelligence.

Funding This study was funded in part by the Zvi Ferminger and wife Hana (Née Cohen, z"l) Fund for Cancer and Dental Research, Faculty of Medicine, Tel Aviv University.

Compliance with ethical standards

Conflict of interest Author Zlotogorski-Hurvitz declares that she has no conflict of interest. Author Dekel declares that he has no conflict of interest. Author Malonek declares that he has no conflict of interest. Author Yahalom declares that he has no conflict of interest. Author Vered declares that she has no conflict of interest.

Ethical approval All procedures performed in studies involving human participants were in accordance with the ethical standards of the institutional research committee and with the 1964 Helsinki declaration and its later amendments or comparable ethical standards.

References

Baker MJ, Gazi E, Brown MD, Shanks JH, Gardner P, Clarke NW (2008) FTIR-based spectroscopic analysis in the identification of clinically aggressive prostate cancer. Br J Cancer 99:1859–1866

Christoua C, Agapioua A, Kokkinoftab R (2018) Use of FTIR spectroscopy and chemometrics for the classification of carobs origin. J Adv Res 10:1–8

Dave N, Lorenz-Fonfria VA, Leblanc G, Padros E (2008) FTIR spectroscopy of secondary-structure reorientation of melibiose permease modulated by substrate binding. Biophys J 94:3659–3670

Dukor RK (2006) Vibrational spectroscopy in the detection of cancer. In: Griffiths P, Chalmers JM (eds) Handbook of vibrational spectroscopy. Wiley, Hoboken, pp 3335–3361

Fantini J, Yahi N (2015) Lipid metabolism and oxidation in neurons and glial cells. In: Fantini J, Yahi N (eds) Brain lipids in synaptic function and neurological disease—clues to innovative therapeutic strategies for brain disorders. Elsevier, Amsterdam, pp 53–85

Ferlay J, Soerjomataram II, Dikshit R, Eser S, Mathers C, Rebelo M et al (2015) Cancer incidence and mortality worldwide: sources, methods and major patterns in GLOBOCAN 2012. Int J Cancer 136:E359–E386

Fushiki T (2011) Estimation of prediction error by using *K*-fold cross-validation. Stat Comput 21:137–146

Gallagher W (2009) FTIR analysis of protein structure. University of Wisconsin web. http://www.chem.uwec.edu/chem455_S05/Pages/Manuals/FTIR_of_proteins.pdf. Accessed 14 July 2018

Gao Y, Huo X, Dong L, Sun X, Sai H, Wei G et al (2015) Fourier transform infrared microspectroscopy monitoring of 5-fluorouracil-induced apoptosis in SW620 colon cancer cells. Mol Med Rep 11:2585–25891

Katsiougiannis S, Chia D, Kim Y, Singh RP, Wong DT (2017) Saliva exosomes from pancreatic tumor-bearing mice modulate NK cell phenotype and antitumor cytotoxicity. FASEB J 31:998–1010

Krafft C, Wilhem K, Eremin A, Nestel S, von Bubnoff N, Schultze-Seeman W et al (2017) A specific spectral signature of serum and plasma-derived extracellular vesicles for cancer screening. Nanomed NBM 13:835–841

Lau C, Kim Y, Chia D, Spielmann N, Eibl G, Elashoff D et al (2013) Role of pancreatic cancer-derived exosomes in salivary biomarker development. J Biol Chem 288:26888–26897

Li Q, Hao C, Kang X, Zhang J, Sun X, Wang W et al (2017) Colorectal cancer and colitis diagnosis using Fourier transform infrared spectroscopy and an improved k-nearest-neighbor classifier. Sensors 17:2739

Lousada-Fernandez F, Rapado-Gonzalez O, Lopez-Cedrun JL, Lopez-Lopez R, Muinelo-Romay L, Suarez-Cunqueiro MM (2018) Liquid biopsy in oral cancer. Int J Mol Sci. https://doi.org/10.3390/ijms19061704

Malamud D (2011) Saliva as a diagnostic fluid. Dent Clin N Am 55:159–178

Mathivanan S, Ji H, Simpson RJ (2010) Exosomes: extracellular organelles important in intercellular communication. J Proteomics 73:1907–1920

Mihaly J, Deak R, Szigyarto IC, Bota A, Beke-Somfai T, Varga Z (2017) Characterization of extracellular vesicles by IR spectroscopy: fast and simple classification based on amide and C–H stretching vibrations. Biochim Biophys Acta Biomembr 1859:459–466

Mohan M, Jagannathan N (2014) Oral field cancerization: an update on current concepts. Oncol Rev 8:244

Moore DT, Berger BW, DeGrado WF (2008) Protein-protein interactions in the membrane: sequence, structural, and biological motifs. Structure 16:991–1001

Palanisamy V, Sharma S, Deshpande A, Zhou H, Gimzewski JK, Wong DT (2010) Nanostructural and transcriptomic analyses of human saliva derived exosomes. PLoS One 5:e8577

Principe S, Hui AB, Bruce J, Sinha A, Liu FF, Kislinger T (2013) Tumor-derived exosomes and microvesicles in head and neck cancer: implications for tumor biology and biomarker discovery. Proteomics 13:1608–1623

Sharma S, Gillespie BM, Palanisamy V, Gimzewski JK (2011) Quantitative nanostructural and single-molecule force spectroscopy biomolecular analysis of human-saliva-derived exosomes. Langmuir 27:14394–14400

Shield KD, Ferlay J, Jemal A, Sankaranarayanan R, Chaturvedi AK, Bray F et al (2017) The global incidence of lip, oral cavity, and pharyngeal cancers by subsite in 2012. CA Cancer J Clin 67:51–64

Simonova D, Karamancheva I (2013) Application of Fourier transform infrared spectroscopy for tumor diagnosis. Biotechnol Biotechnol Equip. 27:4200–4207

Simons M, Raposo G (2009) Exosomes–vesicular carriers for intercellular communication. Curr Opin Cell Biol 21:575–581

Vlassov AV, Magdaleno S, Setterquist R, Conrad R (2012) Exosomes: current knowledge of their composition, biological functions, and diagnostic and therapeutic potentials. Biochim Biophys Acta 1820:940–948

Wong DT, Nonaka T (2018) Liquid biopsy in head and neck cancer: promises and challenges. Crit Rev Oral Biol Med 97:701–708

Zelig U, Mordechai S, Shubinsky G, Sahu RK, Huleihel M, Leibovitz E, Nathan I, Kapelushnik J (2011) Pre-screening and follow-up of childhood acute leukemia using biochemical infrared analysis of peripheral blood mononuclear cells. Biochim Biophys Acta 1810:827–835

Zlotogorski-Hurvitz A, Dayan D, Chaushu G, Korvala J, Salo T, Sormunen R et al (2015) Human saliva-derived exosomes: comparing methods of isolation. J Histochem Cytochem 63:181–189

Zlotogorski-Hurvitz A, Dayan D, Chaushu G, Salo T, Vered M (2016) Morphological and molecular features of oral fluid-derived exosomes: oral cancer patients versus healthy individuals. J Cancer Res Clin Oncol 142:101–110